AIAA JOURNAL
Vol. 48, No. 5, May 2010

Large-Eddy Simulations and Measurements of a Small-Scale High-Speed Coflowing Jet

Simon Eastwood,* Paul Tucker,† and Hao Xia‡
University of Cambridge, Cambridge, England CB3 0DY, United Kingdom
and
Paul Dunkley§ and Peter Carpenter¶
University of Warwick, Coventry, England CV4 7AL, United Kingdom

DOI: 10.2514/1.44534

Measurements and predictions are made of a short-cowl coflowing jet with a bypass ratio of 8:1. The Reynolds number is 300,000, and the inlet Mach numbers are representative of aeroengine conditions. The low Reynolds number of the measurements makes the case well suited to the assessment of large-eddy-simulation-related strategies. The nozzle concentricity is carefully controlled to deal with the emerging metastability issues of jets with coflow. Measurements of mean quantities and turbulence statistics are made using both laser Doppler anemometry and particle image velocimetry. The simulations are completed on 6×10^6, 12×10^6, and 50×10^6 cell meshes. To overcome near-wall modeling problems, a hybrid large-eddy-simulation–Reynolds-averaged-Navier–Stokes-related method is used. The near-wall Reynolds-averaged-Navier–Stokes layer is helpful in preventing nonphysical separation from the nozzle wall.

Nomenclature

A	=	Jacobian, $\partial\Phi/\partial\phi$
A_e, A_μ, c_l, c_μ	=	turbulence model constants
c_v, c_p	=	specific heat capacity at constant volume and constant pressure
D	=	bypass nozzle diameter
d, $\tilde{d}$	=	wall distance and modified wall distance
E	=	total energy per unit volume
e	=	internal energy per unit mass
k	=	turbulent kinetic energy
k_l, k_t	=	thermal diffusivity and turbulent thermal diffusivity
L	=	length scale
l_ε, l_μ	=	modeled turbulence length scales
n	=	integer value
P_{kT}	=	turbulence production term
Pr_T	=	turbulent Prandtl number
p	=	pressure
q	=	heat flux
R	=	gas constant
S_{ij}	=	strain rate tensor
T	=	temperature
T_p T_s	=	primary-flow exit temperature and bypass-flow exit temperature.
t	=	time
t^*	=	nondimensional time
U_p, U_s	=	primary-flow exit velocity and bypass-flow exit velocity.
u, v, w	=	velocity components
x, y, z	=	Cartesian coordinates
y^*	=	Reynolds number
δ	=	Kronecker delta
ε	=	smoothing parameter
ε_0, ε_1	=	tunable constants in Hamilton–Jacobi equation
μ, μ_t	=	viscosity and eddy viscosity
ρ	=	density
σ_k	=	diffusion Prandtl number for k
τ	=	stress tensor
Φ, ϕ	=	flux and primitive variable
$'$	=	fluctuating value
$\tilde{}$, $\langle\,\rangle$	=	time-averaged values

Subscripts

f	=	control-volume face
L, R	=	left- and right-hand nodal values
T	=	distinguishing different values in Reynolds-averaged Navier–Stokes and numerical large-eddy-simulation regions.

Presented as Paper 2981 at the 14th AIAA Aeroacoustics Conference., Vancouver, Canada, 5 May–5 July 2008; received 24 March 2009; revision received 10 February 2010; accepted for publication 10 February 2010.

*Research Associate, Whittle Laboratory, Department of Engineering. AIAA Member.
†Professor of Engineering, Whittle Laboratory, Department of Engineering. AIAA Member.
‡Research Associate, Whittle Laboratory, Department of Engineering.
§Research Associate, School of Engineering.
¶Professor of Engineering, School of Engineering.

I. Introduction

THE propulsive jet from an aircraft engine remains a significant noise source, particularly at takeoff. Hence, with stringent requirements to reduce noise [1], jet noise is an important research area. Turbulent motion in the jet generates noise that propagates to the far field. Hence, understanding jet noise necessarily involves studying complex turbulent flow and understanding jet aerodynamics.

A problem of Reynolds-averaged-Navier–Stokes (RANS) models for jets is that different constants are required in the near and far fields and for different jet-flow types [2]. No satisfactory solution to this has been found in the last 30 years. However, the major issue for RANS-based predictions is not calculating the mean flow but noise predictions. Because of their implicit time averaging, RANS-based approaches remove the spectral information needed for noise predictions.

Large-eddy simulation (LES) provides an alternative to RANS that can, even on quite coarse grids [3,4], predict correct trends. As discussed by Pope [5], a compelling case for the use of LES can be

made for momentum, heat, and mass transfer in free shear flows. In this case, the transport processes of interest are effected by the resolved large-scale motions with a cascade of energy from the resolved large scales to the statistically isotropic and universal small scales. LES is useful for jet aerodynamics and ultimately noise predictions, because spectral information of the larger scales is resolved for. In jet shear layers, small scales have little influence on the large [6], suggesting the modeling of back scatter (as facilitated by more advanced LES models) is relatively unimportant. In a turbulent jet, most downstream noise is generated by large structures at the tip of the potential core. Therefore, there are strong reasons to expect LES to be successful in, for example, capturing the major noise sources. Several studies have proven the potential of LES for jets [4,7–13]. The status of jet predictions using LES are reviewed in [14]. The majority of these simulations do not include the nozzle geometry in the domain; an imposed velocity profile is preferred instead. This is primarily done for convenience and simplicity, as including the nozzle would make calculations costly due to near-wall modeling issues.

Many industrial computational-fluid-dynamics (CFD) solvers naturally display dissipative qualities [15]. Also, low-order numerical discretizations can be as influential as the subgrid scale (SGS) model [16,17]. This means it can be difficult to disentangle the effect of numerics and SGS modeling. Because the code being used here (as with the majority of industrial-based solvers) tends toward being dissipative, omitting the SGS model can be helpful; otherwise, excessive dissipation can occur [3]. Model free computations can be termed implicit LES (ILES) and have been shown to capture some complex jet dynamics well [12]. The nature of the ILES approach is fully detailed in [18]. It uses monotone schemes to provide appropriate levels of numerical viscosity to replace that of the SGS model. Shur et al. [3] successfully use ILES-reminiscent simulations for jet predictions. In the current work, the SGS model is also omitted. However, following Pope [5], the term numerical LES (NLES) is used rather than ILES. The implication being that the numerical elements of the scheme are significantly active, no claim being made that the numerical contributions represent an especially good SGS model.

More recently, there has been work toward coupling the jet plume to the explicit nozzle geometry. Examples of this include, amongst others, axisymmetric flows [7,19–21], coflowing [22–27], and bevelled [28,29] and chevron [30,31] jets. Modeling the nozzle boundary layer is challenging; for example, there are numerous small near-wall streaklike structures. These require fine, computationally expensive, cross-stream grids. Hybrid LES–RANS-type approaches are useful, as they can accurately capture the bulk properties of the boundary layer and circumvent the near-wall streak resolution issues. Perhaps the most common realization of this is the detached-eddy-simulation (DES) method [32]. In the current work, a k–l [33] near-wall RANS model is used, with NLES being used away from walls. The method circumvents near-wall streak resolution issues. The disparate-length scales in the two zones are blended using a (differential) Hamilton–Jacobi (HJ) equation. This approach has been used before to explore simple jets and also chevron nozzles [13,21,34]. Here, the previously validated method is extended to explore more complex coflowing jets.

In addition to the modeling issues of LES, for fluid dynamics in general, practitioner expertise is still required, and the triad of computation, measurement, and analytical solution must be judiciously used. For this triad to be successful, measurements must yield uncontaminated turbulent statistic data. For jets, boundary layers are generally much thinner than can be modeled using many LES strategies. This makes serious assessment of numerical modeling difficult. Also, nominally axisymmetric coaxial flows can be very sensitive to small nozzle distortions [35], potentially rendering much past data for this configuration questionable. It has taken a surprisingly long time for this to come to light. However, this aligns with other work [36,37] that strongly advocates the need to model real geometry influences. Here, a small-scale nozzle system is used that negates modeling realistic engine conditions. Also, the inlet conditions are not representative of those found on a real engine (lower Reynolds number and isothermal). However, the rig provides valuable data for computer model validation, and the study offers the opportunity for a direct and detailed comparison of calculations and experiments. At present, for much of the computational work carried out in the field of jet noise, there is a lack of detailed measurements to provide validation and even basic understanding of the flow physics [38], hence making this work important.

Recently, pioneering particle image velocimetry (PIV) work has been carried out for a single-stream nozzle [39,40]. Such data can be used to develop and validate improved jet-flow-prediction procedures, as discussed by Birch et al. [35]. In the current work, PIV and laser Doppler anemometry (LDA) measurements are presented for a coflowing nozzle geometry. Both streams are isothermal, eliminating expansion and contraction problems associated with metal heating, which may exaggerate the symmetry issues previously mentioned.

II. Numerical Method

A. Governing Equations

The Navier–Stokes equations are solved in their compressible form. Hence, conservation of momentum can be expressed using

$$\frac{\partial \rho \tilde{u}_i}{\partial t} + \frac{\partial \rho \tilde{u}_i \tilde{u}_j}{\partial x_j} = -\frac{\partial \tilde{p}}{\partial x_j} + \frac{\partial \tilde{\tau}_{ij}}{\partial x_j} \tag{1}$$

where $\tilde{u}_i$ is fluid velocity, ρ is density, μ is viscosity (evaluated from Sutherland's equation), $\tilde{p}$ is static pressure, t is time, and x is the spatial coordinate. The stress tensor $\tilde{\tau}_{ij}$ is given by

$$\tilde{\tau}_{ij} = 2(\mu + \mu_T)\left[\tilde{S}_{ij} - \frac{1}{3}\frac{\partial \tilde{u}_j}{\partial x_j}\delta_{ij}\right] \tag{2}$$

where δ_{ij} is the Kronecker delta. The strain-rate tensor is expressed as

$$\tilde{S}_{ij} = \frac{1}{2}\left(\frac{\partial \tilde{u}_i}{\partial x_j} + \frac{\partial \tilde{u}_j}{\partial x_i}\right) \tag{3}$$

The tilde and the T subscript in the previous equation help identify that near-wall traditional RANS averaging is assumed and that, elsewhere, NLES is implemented. Hence, in the RANS region, $\mu_T = \mu_t$, the eddy viscosity. In the NLES region, effectively, μ_T is the numerical diffusion. Along with the previous equation, the following energy equation is solved,

$$\frac{\partial \tilde{E}}{\partial t} + \frac{\partial}{\partial x_j}[\tilde{u}_j(\tilde{E} + \tilde{p})] = \frac{\partial}{\partial x_j}(\tilde{u}_i \tilde{\tau}_{ij}) - \frac{\partial \tilde{q}_j}{\partial x_j} \tag{4}$$

with the total energy per unit volume expressed as

$$\tilde{E} = \rho e + \tfrac{1}{2}\rho \tilde{u}_i \tilde{u}_i \tag{5}$$

In the previous equation $e = c_v \tilde{T}$, where c_v is the constant volume specific heat. Pressure, temperature, and density are related through the equation of state for a perfect gas, $\tilde{p} = \rho R \tilde{T}$. For the heat flux $\tilde{q}$, the following is used:

$$\tilde{q} = -(k_l + k_T)\frac{\partial \tilde{T}}{\partial x_j} \tag{6}$$

In the previous equation, k_l is the thermal conductivity and $k_T = c_p \mu_T / Pr_T$, where c_p is the specific heat at constant pressure and Pr_T is the turbulent Prandtl number. It follows that, in the NLES zone, because $\mu_T = 0, k_T = 0$. The continuity equation to go with the previous equation is

$$\frac{\partial \rho}{\partial t} + \frac{\partial \rho \tilde{u}_j}{\partial x_j} = 0 \tag{7}$$

B. Near-Wall Modeling

An LES practice is to take the modeled turbulence length scale as $\min(C_s\Delta, \kappa y)$ [41], where C_s and κ are the Smagorinsky and Karman constants, respectively. For an LES-type grid, this will

introduce (mixing length) RANS modeling for $y^+ \ll 60$. Here, to reduce grid demands but still maintain the higher-LES fidelity, we switch between RANS and NLES at $y^+ \approx 60$, covering over just the near-wall streak structures having the finest scales. Hence, the switch is much closer to the wall than for DES (for which the whole boundary layer is RANS modeled) but further out than for LES. Validation of the current approach can be found in [13,42,43]. Different values of y^+ for a jet with coflow are explored in [42]. For an interface at $y^+ < 60$, the law of the wall was not captured properly. Hence, here, the y^+ value of 60 is chosen. This allows the fullest extent of the NLES region while capturing the law of the wall.

For the near-wall RANS region, the k–l model [33] is used. Following Shur et al. [25], and to save computational time, the developed RANS layer is generally frozen. The modeled turbulent kinetic energy k equation is as follows,

$$\frac{\partial \rho k}{\partial t} + \frac{\partial \rho u_i k}{\partial x_i} = \frac{\partial}{\partial x_j}\left[\left(\mu + \frac{\mu_t}{\sigma_k}\right)\left(\frac{\partial k}{\partial x_j}\right)\right] + P_{kT} - \frac{\rho k^{3/2}}{l_\varepsilon} \tag{8}$$

where P_{kT} is the turbulence production term. In the NLES region, $k = 0$. For the RANS region, then

$$\mu_t = \rho C_\mu l_\mu k^{1/2} \tag{9}$$

where the length scale of Eq. (9) is given by

$$l_\mu = C_l \tilde{d}(1 - e^{-A_\mu y^*}) \tag{10}$$

and the length scale of Eq. (8) is given by

$$l_\varepsilon = C_l \tilde{d}(1 - e^{-A_\varepsilon y^*}) \tag{11}$$

and $y^* = \tilde{d}\rho k^{1/2} C_\mu^{1/4}/\mu$. Constants have the following standard values: $C_\mu = 0.09, C_l = 2.4, A_\mu = 0.016, A_e = 0.263$, and $\sigma_k = 1.0$ (the diffusion Prandtl number for k).

For the RANS region, the exact wall distance d is required, whereas in the NLES region, d is zero. Hence, a separate variable $\tilde{d}$ is defined, where in the RANS region, $\tilde{d} = d$, and in the NLES region, $\tilde{d} = 0$. The distance function $\tilde{d}$ is evaluated from the HJ equation:

$$|\nabla \tilde{d}| = 1 + f(\tilde{d})\nabla^2 \tilde{d} + g(d) \tag{12}$$

The first two terms of Eq. (12) give the eikonal equation, which gives the d needed for the RANS zone. The blending between the RANS and LES zones is achieved by the addition of a Laplacian (given by the third term). In Eq. (12), $f(\tilde{d}) = \varepsilon_0 \tilde{d}$ and $g(d) = \varepsilon_1 (d/L)^n$. The length scale L is the distance from the wall to the NLES region, and n is a positive integer. The function $f(\tilde{d})$ forces the Laplacian to tend to zero near walls. The function $g(d)$ helps to bias the blending. Figure 1 shows various distributions that can be formed for different ε_0 and ε_1. The HJ equation can either be solved for directly in HYDRA code or a polynomial fit to a particular distribution can be used to control $\tilde{d}$. The latter option is used here with $n \simeq 4$, $\varepsilon_0 \simeq 1.2$, and $\varepsilon_1 \simeq 7.5$. The RANS layer is also cropped at the nozzle-exit plane, so that the RANS layer does not extend into the shear layer. The influence of different values for n, ε_0, and ε_1 are explored in [13]. Results were found to be relatively insensitive to the precise smoothing parameters used. Hence, here, a smoothing profile that lies in the middle of the range explored in [13] is used.

C. Solution of the Governing Equations

The unstructured, cell vertex, Rolls–Royce Group, PLC HYDRA code [15] is used for the calculations. The flux at the control-volume interface is based on the flux difference ideas of Roe [44]. The inviscid flux at a control-volume face Φ_f is expressed as

$$\Phi_f = \tfrac{1}{2}(\Phi_L + \Phi_R) - \tfrac{1}{2}|A|[\phi_L - \phi_R] \tag{13}$$

where $A = \partial\Phi/\partial\phi$ (ϕ represents primitive variables), and the subscripts L and R represent variables based on information to the left- and right-hand side of the face. Here, Φ_L and Φ_R are simply taken as the adjacent nodal values [45] (i.e., $(\Phi_L + \Phi_R)/2$ represents a standard second-order central difference). The smoothing term is also approximated in a second-order fashion as

$$\tfrac{1}{2}|A|[\phi_L - \phi_R] = \tfrac{1}{2}\varepsilon|A|[\tilde{\nabla}_L^2 \phi - \tilde{\nabla}_R^2 \phi] \tag{14}$$

where $\tilde{\nabla}_L^2$ and $\tilde{\nabla}_R^2$ are undivided Laplacians evaluated at the node locations L and R. The constant ε is tunable, with the standard HYDRA value being 0.5. Following Shur et al. [3], the ε term has the static spatially varying distribution shown in Fig. 2. To help prevent reflection of spurious waves, the smoothing is a minimum in the most active turbulent regions and increases toward the domain boundaries. To aid stability, smoothing is also increased at the nozzle exit. Too low a value of ε is not helpful for accuracy, because the dispersion error becomes significant. The term $|A|$ in Eq. (13) involves differences (and summations) between the local convection velocity and speed of sound. As the Mach number tends to unity, key terms in $|A|$ become small. However, near walls, $|A|$ becomes large. This will contaminate the LES scales but (here) helpfully, they are covered by the RANS layer. For the temporal discretization, an explicit five-stage Runge–Kutta scheme is used.

As shown in [46], the numerical viscosity for the current scheme (for homogeneous decaying turbulence) is of the same order of magnitude as that provided by the Smagorinsky SGS model. This is consistent with the expectations of Ghosal [17] and Kravchenko and Moin [16] that show that, for a second-order numerical scheme and a standard filter size, the numerical contribution will dominate that of the LES model.

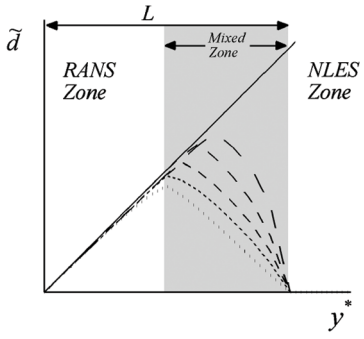

a) Wall distance function between RANS and NLES regions

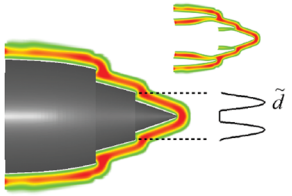

b) Contours of modified wall distance around geometry

Fig. 1 Illustrations of wall distance function; RANS layer thickness is magnified to 0.1*D* for clarity (dots: $\varepsilon_0 = 1.2$ and $\varepsilon_1 = 0.0$; small bold dashes: $n = 4$, $\varepsilon_0 = 1.2$, and $\varepsilon_1 = 1.5$; dashes: $n = 4$, $\varepsilon_0 = 1.2$, and $\varepsilon_1 = 3.5$; longer dashes: $n = 4$, $\varepsilon_0 = 1.2$, and $\varepsilon_1 = 7.5$; longest dashes: $n = 9$, $\varepsilon_0 = 1.2$, and $\varepsilon_1 = 35.0$).

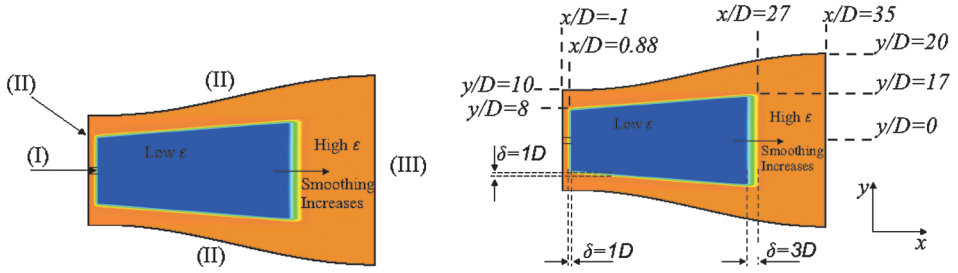

a) Variation of smoothing function and boundary conditions

b) Location of the boundary conditions

Fig. 2 Imposed boundary conditions and variation of smoothing factor ε, showing lower smoothing and the highest smoothing.

D. Geometry and Mesh

The Fig. 3 geometry is reminiscent of the short-cowl nozzle used in the European Union coaxial jet-noise prediction program (COJEN). Figure 4 shows the mesh in the x–y plane and also in the y–z plane at $x/D = 1$. Three meshes are used with 6×10^6, 12×10^6, and 50×10^6 cells. To help avoid skewness issues, which can result in severe dissipation, hexahedral body-fitted meshes with a multiblock topology are preferred [47]. Furthermore, meshes that maintain orthogonality between the control-volume face and the line that connects the nodes that straddle that face tend to give better energy-conservation properties [48]. The first offwall grid node is set at an average of $y^+ = 1.0$ for all meshes. This is more than adequate for the k–l model, with its algebraically prescribed length scale and a first offwall grid location of $4 \times 10^{-5}D$. The nozzle has a blunt nose. Here, an H Block is embedded to avoid an axis singularity on the jet centerline.

For the 12×10^6 cell case, there are 60 nodes, radially, in both the core and bypass flows. Axially, from the bypass inlet to the nozzle tip, there are 100 nodes. From the nozzle tip to $x/D = 4$ are another 150 nodes. There are 150 azimuthal nodes, giving a total (in this region) of 4.5×10^6 cells. This gives Δx^+ and Δr^+ values of 300 and 150 in the nozzle at the bypass and core exits. A further 4.5×10^6 are used from $x/D = 4$ to 8. The remaining nodes are used further downstream and radially outside the nozzle. At $x/D = 1$ (the nozzle tip is at $x/D = 0.88$), there are about 30 nodes across the outer shear layer and roughly 35 nodes across the inner shear layer. At $x/D = 3$, the shear layers have merged to form one shear layer. Here, there are (in the region) about 40 grid points across the shear layer.

For the 6×10^6-cell mesh, the grid topology is the same, but the grid count is reduced by around 75% in all directions. For the 50×10^6-cell mesh, the 6×10^6-cell mesh is approximately doubled in all directions.

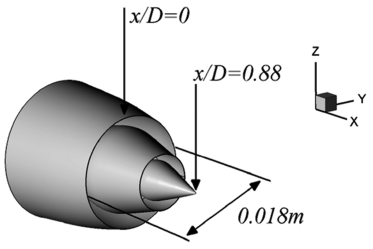

Fig. 3 Short-cowl coflowing nozzle.

E. Boundary Conditions

The operating conditions are summarized in Table 1. The Reynolds number Re is 300,000 (based on the nozzle diameter D and maximum jet velocity in the bypass flow U_s). The exit Mach numbers are matched to those of a real jet engine, with the exit velocity of the core and bypass at 240 ms^{-1} and 216 ms^{-1}, respectively. The boundary conditions are labeled in Fig. 2a. Both the core and bypass inlets (boundary I) are prescribed as subsonic inlets. Partly motivated by not wanting to introduce spurious waves, no forcing is applied. This also prevents the introduction of arbitrary parameters. No velocity profiles are specified at the nozzle inlet. The boundary layers develop naturally to give boundary-layer thicknesses of around $0.02D$ for both the core and bypass nozzle exits. For the measurements, a large plenum feeds flow into channel-like zones. Turbulent boundary layers develop in these relatively long ($3 \sim 4D$) thin ($0.25D$) channels, giving nozzle-exit boundary-layer thicknesses of approximately $0.015D$ for both the core and bypass flows. This estimate is based on use of the Blasius and one-seventh-power laws and the von Karman integral momentum equation to derive an expression for boundary-layer thickness. Hence, the boundary-layer thicknesses of the measurements and computations are expected to be broadly the same. For the 50×10^6-cell case, sponge zones were implemented at boundary I to prevent spurious reflections at the inflow. These reflections occurred, due to the increased mesh density at the inlet supporting acoustic waves propagating upstream from the shear layer.

At boundary III, a subsonic outlet is prescribed. This boundary is located $35D$ downstream of the jet exit. At boundary II, a freestream condition is used. Near to the boundaries, the smoothing is increased to help prevent reflection of spurious waves. Figure 2b shows the

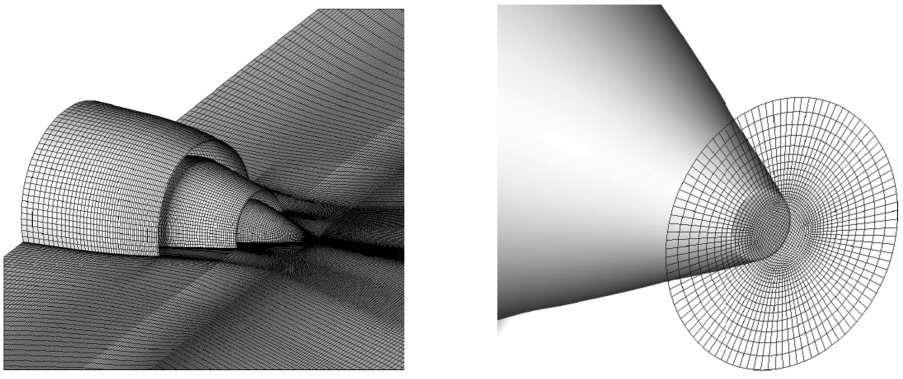

Fig. 4 Mesh images around the nozzle and in the x–y plane (left) and in the y–z plane (right).

Table 1 Jet flow conditions

Parameters	Values
Velocity of primary flow, U_p	240 ms^{-1}
Velocity of bypass flow, U_s	216 ms^{-1}
Static temperature in primary flow, T_p	300 K
Static temperature in bypass flow, T_s	300 K

Table 2 LDA control volume sizes, mm

Volume side	Beam 1	Beam 2
dx	0.1248	0.1183
dy	0.1244	0.1180
dz	1.684	1.597

domain boundaries and where the smoothing increases. The distance over which the smoothing increases is given by δ. Also, the nozzle walls are viscous.

F. Solution Time

The simulation is run from quiescent initialization. For the 12×10^6-cell mesh, the physical time step of the simulation is approximately 0.2×10^{-8} s, based on the smallest cell size. This gives a maximum Courant–Friedrichs–Lewy number of approximately 0.5 in the near-nozzle region. Based on the bypass-jet diameter and peak velocity, this gives t^* of approximately 3×10^{-5}. Hence, a single t^* requires 35,000 physical time steps. The solution runs on a Cray *XT*4 computer comprising 1416 compute blades, which each have four quad-core processors. This amounts to a total of 22,656 cores. The system uses Advanced Micro Devices (AMD) 2.3 GHz Opteron processors, giving a theoretical peak performance of 208 tflop. Using 128 cores, approximately 75,000 time steps can be completed in 12 h. A mature solution is gained over $100t^*$ and averaged over a further $100t^*$. Hence, the complete simulation takes approximately 2 months.

For the same number of cores, the 6×10^6 mesh takes approximately one month to complete. For the 50×10^6-cell mesh, the case is run using 256 cores. However, the smaller time step ($\sim 0.5 \times 10^{-9}$) results in the simulation requiring approximately 200 days of run time to obtain time-averaged results. It is worth noting that these times are for an unstructured solver, which gives a substantial overhead relative to a structured solver. To reduce the time to gain a mature flow solution, flow from the 12×10^6-cell mesh is interpolated onto the 50×10^6-cell mesh. Also, for the 50×10^6-cell mesh, results are averaged azimuthally across eight equally spaced planes.

III. Experimental Technique

The jet rig is housed in the center of a $4 \times 4 \times 3$m anechoic chamber. It is supplied with air from a single reservoir located outside of the chamber via a plenum chamber. A second compressor and reservoir are used to supply air to the seeding system to produce particles for the LDA and PIV measurements. The current arrangement provides enough air for approximately 30 min. of continuous running. Laser experiments showed the seeding to be fully mixed. The seeding used is corn oil, giving particles of approximately 1 μm in diameter and a frequency response of 10 kHz.

Flowfield measurements have been taken with a Dantec two-dimensional LDA system. To allow higher data rates while running in coincidence, the LDA head was rotated 45 deg. Running in coincidence was required to provide Reynolds stress values. An average data rate of 8.5 kHz was achieved at 5D downstream, with a peak of 19 kHz. Data were captured in a polar coordinate system for the planes normal to the principal-flow direction, with 10,000 data points per position and 156 positions.

The relative statistical error for convergence of the basic LDA measurements is just 0.02%. Based on the data rate and the convective velocity, enough data are collected to gain an averaging period of approximately $50t^*$. The control-volume sizes associated with the two LDA beams are give in Table 2. Although the precision

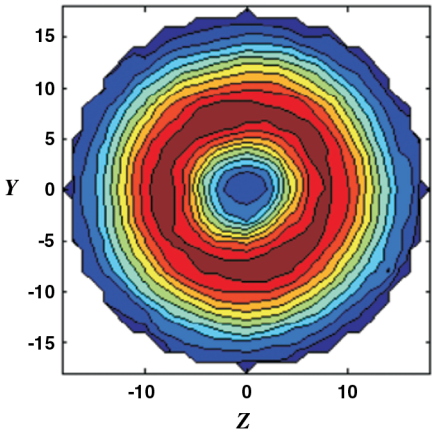

Fig. 6 y–z plane of normal stress from LDA measurements at $x/D = 5.0$.

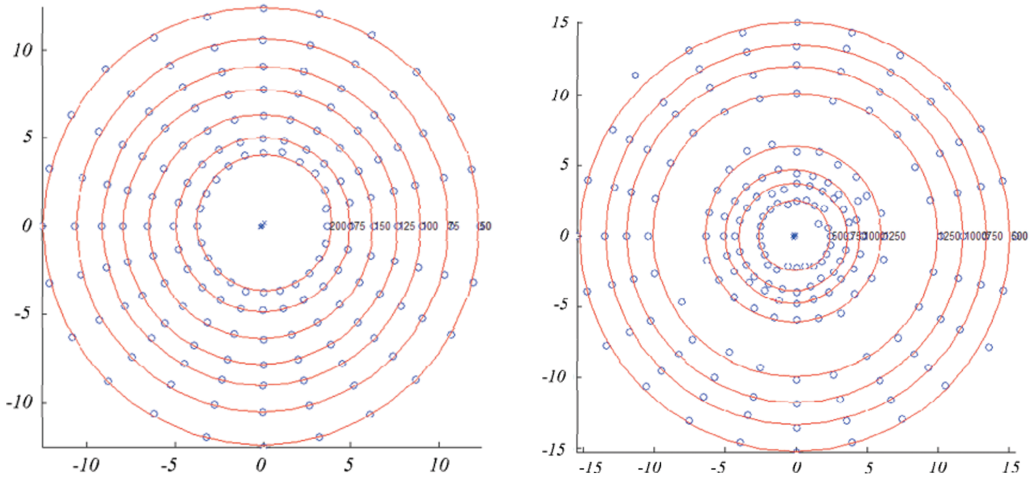

a) Mean streamwise velocity **b) Normal stress**

Fig. 5 Circle fitting (for which the symbols are measurements, the lines are circle fits, and the crosses are derived circle centers).

Table 3 Average error (in %) between the measurements and 12 × 10^6-cell RANS–NLES

Error	$x/D = 3$	$x/D = 4$	$x/D = 5$
Error_U	6.5	8	10
$\text{Error}_{\overline{u'u'}}$	39	30	22
$\text{Error}_{\overline{u'v'}}$	18	27	17
$\text{Error}_{\overline{v'v'}}$	15	20	20

of the basic LDA measurements is high (less than 1% error), there is a substantial uncertainty (up to 5%) in traverse position location.

Cross-sectional results were used to verify the symmetry of the jet, using circle-fitting techniques. Figure 5 shows the circle-fitting technique for the mean streamwise velocity (Fig. 5a) and for the normal stress (Fig. 5b). Symbols show measurements at constant values (of velocity or normal stress) around the circumference of the jet. Different velocities and stresses are investigated, giving different radial locations. Using a least-squares technique, circles are fitted through the points (shown by the solid lines). The center of the fitted circles is then derived and compared with the true center point. Calculated jet-center positions, based on the circle fitting, varied less than 1 mm, even at $10D$. So, for $1D = 18.0$ mm, this corresponds to a 5.5% error in the shear-layer location. Figure 6 shows a contour plot of the Reynolds stress at $x/D = 5.0$ for the LDA results. This demonstrates the flow to be sensibly axisymmetric.

However, without careful concentricity control, the jet had the propensity to exhibit nonconcentricity (even though isothermal).

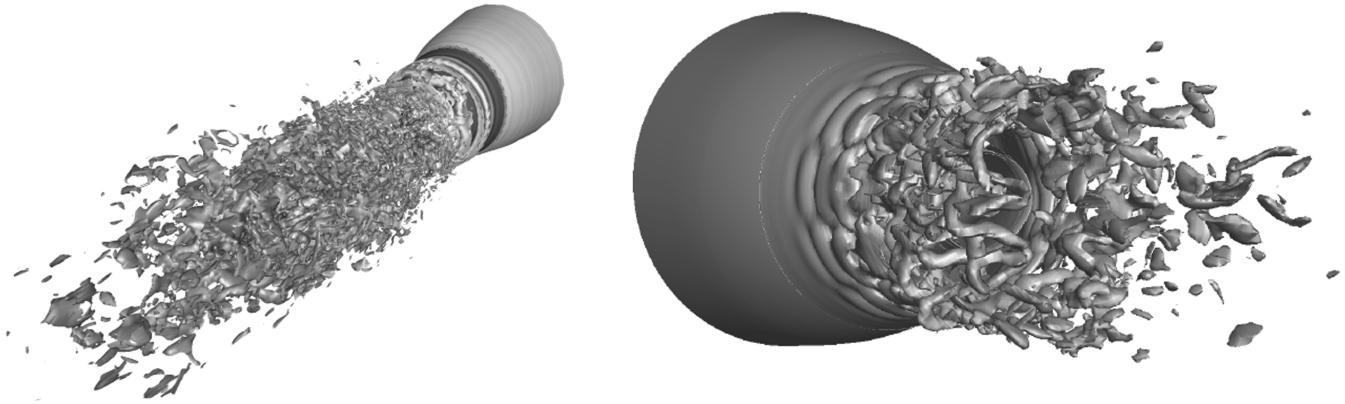

Fig. 7 Vorticity isosurface images for the 12 × 10^6 case.

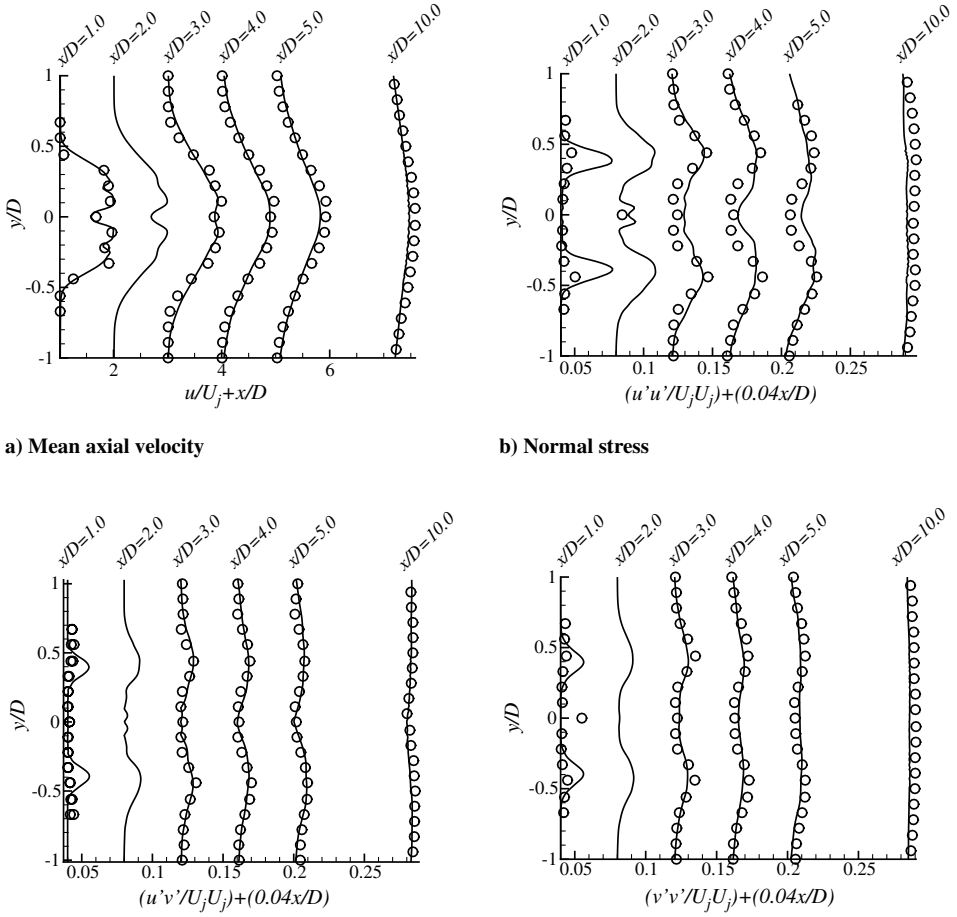

a) Mean axial velocity **b) Normal stress**

c) Shear stress **d) Radial stress**

Fig. 8 Radial profiles at axial locations $x/D = 1.0$, 2.0, 3.0, 4.0, 5.0, and 10.0 (lines: NLES–RANS; circles: LDA measurements).

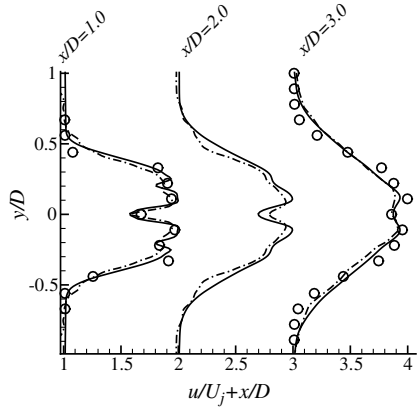

a) Mean axial velocity

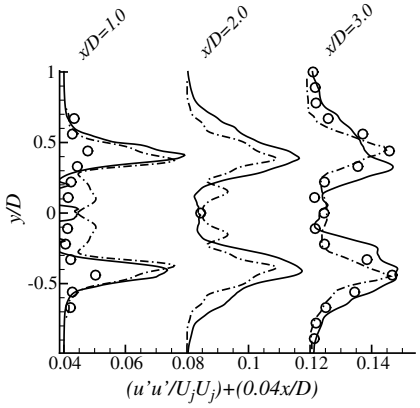

b) Normal stress

Fig. 9 Radial profiles at axial locations $x/D = 1.0$, 2.0, 3.0, 4.0, and 5.0 (dashes: 6×10^6 NLES–RANS; dashes/dots: 50×10^6 NLES–RANS; circles: LDA measurements).

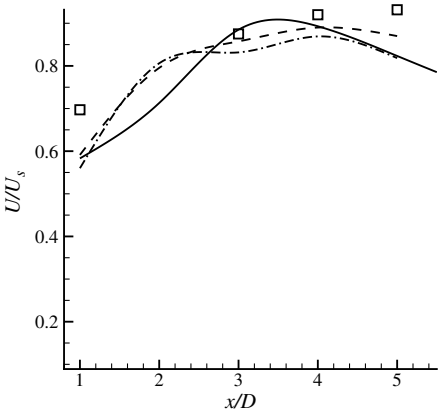

a) Centerline time-averaged streamwise velocity

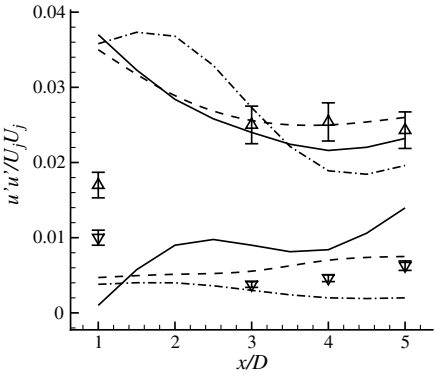

b) Peak normal stress (upper curves) and centerline normal stress (bottom curves)

Fig. 10 Axial profiles (top set of curves is peak values, and bottom set of curves is on centerline). (Symbols: LDA measurements; dashes/dots: 6×10^6, lines: 12×10^6; dashes: 50×10^6).

This concentricity problem for hot jets is well outlined by [35], as noted earlier. During the extensive measurement periods, there is no guarantee that concentricity deviations did not (periodically) occur. This seems to manifest itself most in the Reynolds stress distributions. For mean velocities, the potential concentricity error is negligible. However, for the stresses (without careful alignment), values could be laterally displaced by 5% at $x/D = 5$ (the displacement having a roughly linear distribution with x). Factoring in possible maximum concentricity deviations during runs suggests another 5% error in Reynolds stresses in the focus zone of this work ($x/D < 5$). Hence, the overall error is up to 10%, due to positional and jet stability issues [the base LDA measurements being accurate (1% error) by comparison]. However, projecting back the shear-layer half-width (estimated on $\overline{u'u'}$) for $x/D < 1$, the shear-layer thickness is comparable with the measurement volume. Hence, error estimates are not shown for $x/D < 1$.

PIV measurements were taken using a PCO 2000 (2048× 2048 pixels) camera and an Oxford Lasers dual-head neodymium–doped-yttrium-aluminum-garnet (532 nm) laser. The data were processed using LaVision's DaVis software. The area viewed was approximately $2.5D \times 2.5D$, giving 37 pixels/mm. A pulse separation of 2 μs was used for all the PIV. Multipass processing was implemented in the DaVis software, with a starting interrogation window of 128×128, finishing with 16×16 pixel. 1000 frame pairs were recorded to provide the scaler results presented.

As is well known, PIV measurements are good for capturing structures in the flow, but they are not as good for absolute values. Problems with obtaining accurate PIV include spatial resolution in terms of the interrogation window and laser sheet thickness. Hence, the LDA point measurements are regarded as being the most accurate (less than 10% error). However, the PIV is useful for capturing the qualitative features of the flow and should be regarded as flow visualization.

For comparing the error of measurements to the predictions, the following experimental data-point summations are made,

$$\text{Error}_{\phi} = \frac{\Sigma|\Phi_{\text{exp}} - \Phi_{\text{num}}|}{\Sigma(|\Phi_{\text{exp}}|)} \tag{15}$$

Table 4 Summary of errors (in %) at $x/D = 3$ for all simulations and measurements. Values in brackets show error in the peak values

	Grids				
	6×10^6	12×10^6	50×10^6	$\Delta_{\max}$ between CFD	$\text{Error}_{\text{measurements}}$
Error_U	4.5	6.5	7.5	3	±5.5
$\text{Error}_{\overline{u'u'}}$	21 (4.2)	39 (8)	26 (3.8)	18 (4.2)	±10

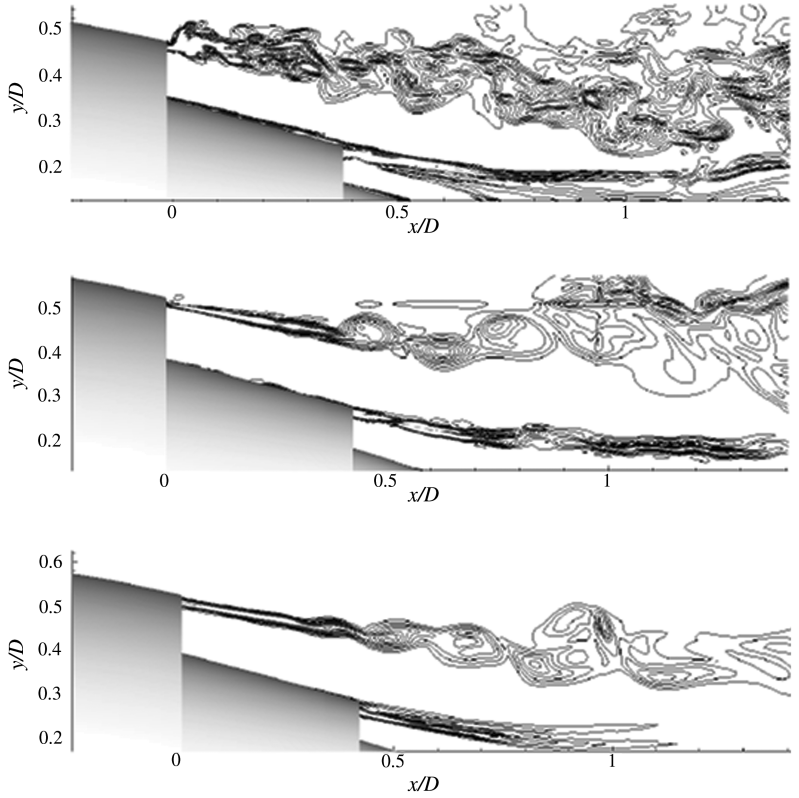

Fig. 11 ***x–y*** **contours of vorticity for different mesh densities. Top frame shows 50 × 10^6-cell mesh, middle frame shows 12 × 10^6-cell mesh, and bottom frame shows 6 × 10^6-cell mesh.**

where Φ is the mean streamwise velocity or turbulence intensity, and the subscripts num and exp refer to LES predictions and measurements, respectively. At points where numerical data points do not coincide exactly with the measurements, a stiff quadratic spline interpolation is used. Error_ϕ gives an average error across the radial profile. For a difference in error of two LES predictions, the same data-point locations are used as for the measurements. Subscripts num and exp are replaced by LES_1 and LES_2, which refer to two LES predictions. In the Eq. (15) denominator, Φ_{exp} is replaced by the average of the two CFD predictions. Errors in mean streamwise velocity and normal stress are shown later in Table 3.

IV. Results

To gain an initial visual impression of the flow, Fig. 7 plots vorticity isosurfaces from the 12 × 10^6-cell NLES–RANS solution. A wide range of scales with substantial anisotropy can be observed.

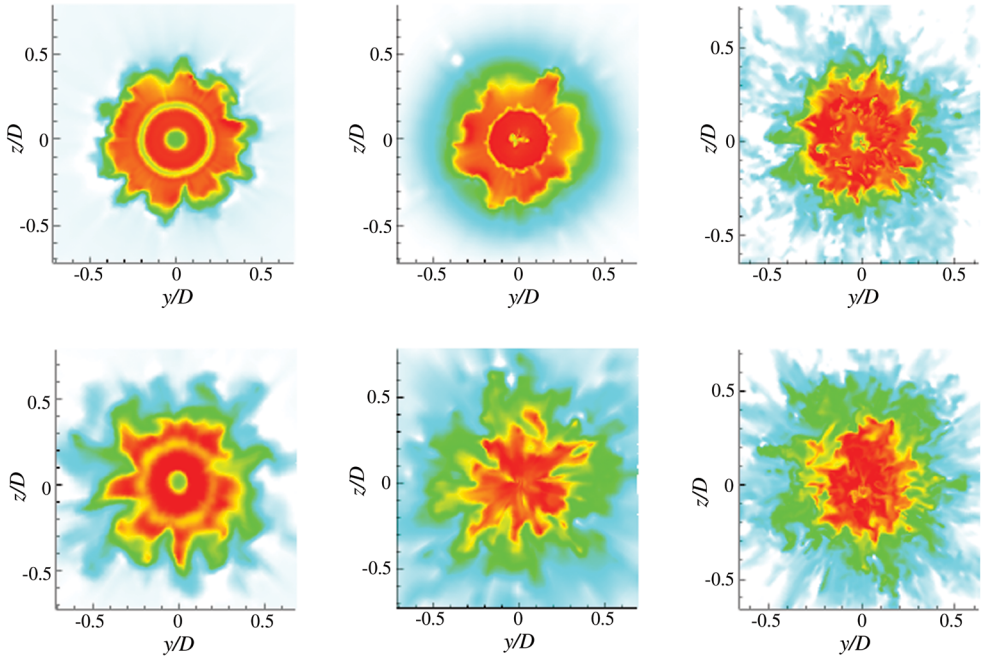

Fig. 12 ***y–z*** **contours of streamwise instantaneous velocity for different mesh densities. Top row shows axial profiles at $x/D = 1$ and bottom row at $x/D = 2$. Left to right frames show 6 × 10^6-cell, 12 × 10^6-cell, and 50 × 10^6-cell mesh results, respectively.**

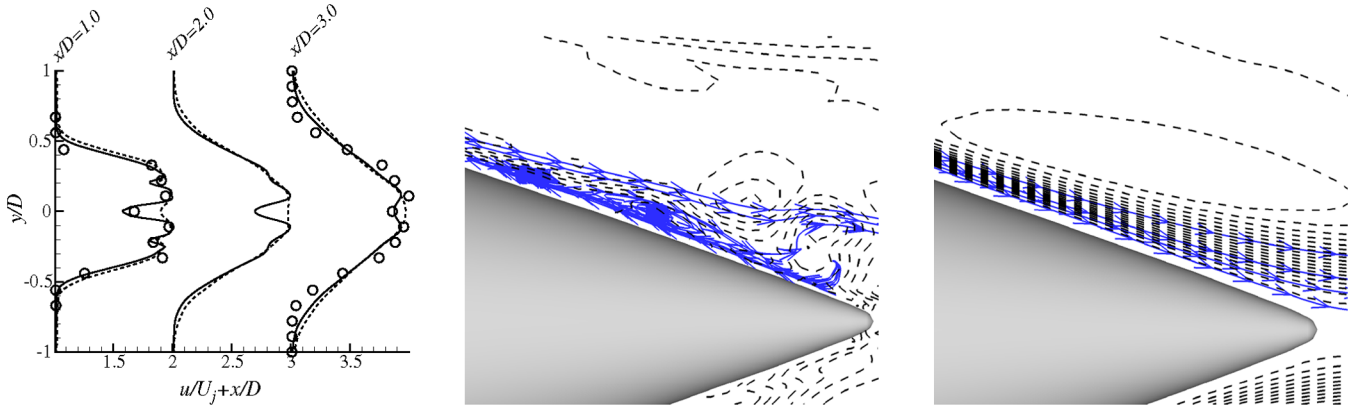

a) Mean axial velocity **b) Without near wall RANS** **c) With near wall RANS**

Fig. 13 Comparison of NLES–RANS and NLES: a) radial profiles of mean axial velocity at $x/D = 1.0, 2.0$, and 3.0 (lines: NLES–RANS; dashes: NLES; circles: LDA measurements); b) NLES flowfield; and c) NLES–RANS flowfield (dashes: density gradient magnitude contours; lines: instantaneous streamlines).

In the following graphs, time-averaged velocity quantities are normalized by the peak streamwise velocity U_j. Reynold's stresses are normalized by the peak streamwise velocity squared. Radial profiles extracted at different axial locations (x/D) are plotted on the same graph (for the same quantity). The profiles are offset axially by a constant multiplied by x/D, so that they are not overlaid. For the time-averaged velocity plots, the multiplying constant is one, and for the Reynolds stress plots, it is 0.04, as identified on the graph axes.

Figure 8 plots radial profiles of mean streamwise velocity and normal, shear, and radial stresses at axial locations of $x/D = 1.0, 2.0$, 3.0, 4.0, 5.0, and 10.0. Full lines show the 12×10^6-cell NLES–RANS results and symbols show the LDA measurements. For the

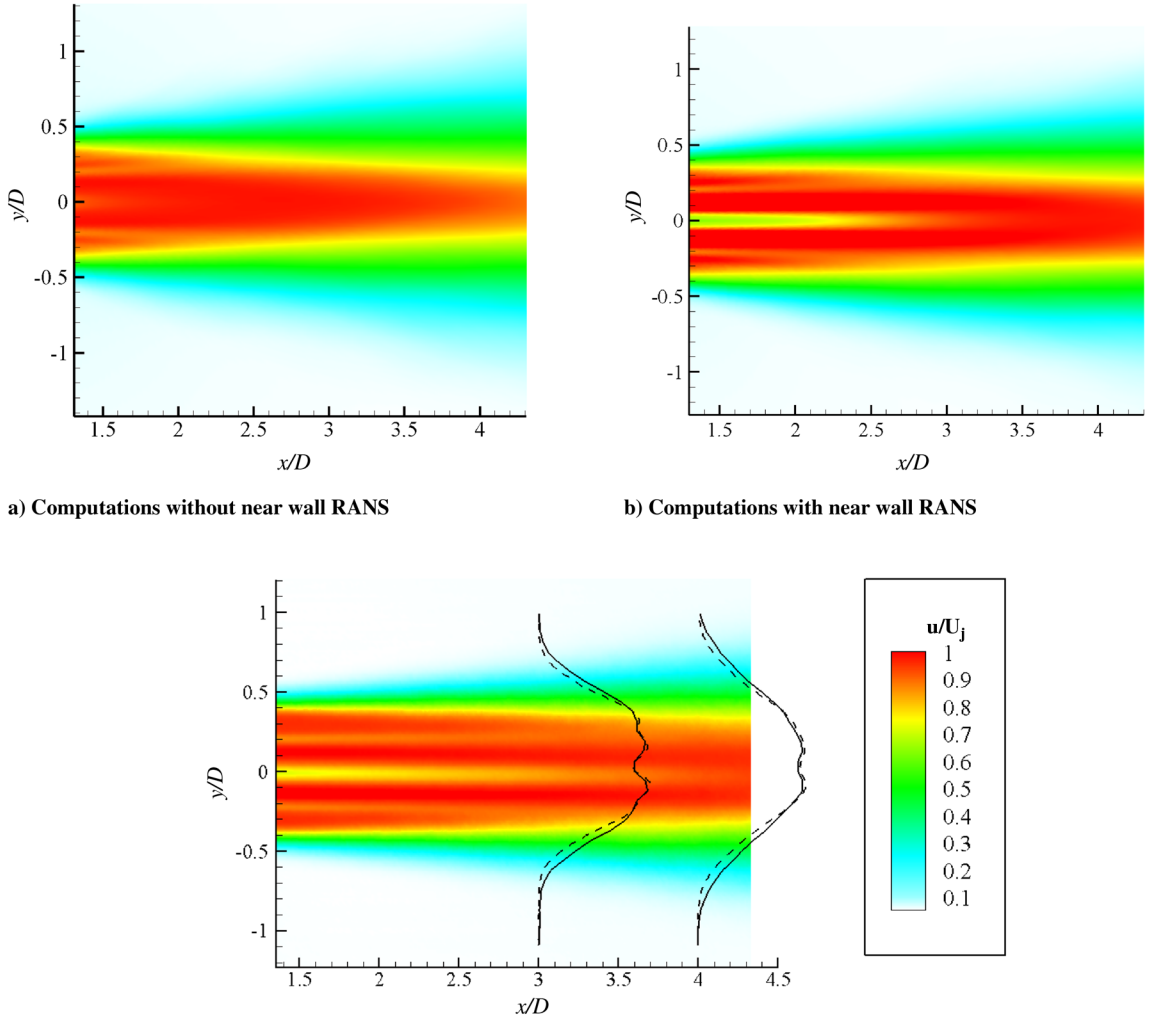

a) Computations without near wall RANS **b) Computations with near wall RANS**

c) PIV measurements

Fig. 14 Contours in x–y plane of time-averaged streamwise velocity: a) NLES, b) NLES–RANS, and c) PIV. Overset lines show radial profiles of time-averaged streamwise velocity at axial locations $x/D = 3$ and 4 for LDA (lines) and PIV (dashes).

axial velocity, shown in Fig. 8a, there is encouraging agreement between the computations and measurements. At $x/D = 5.0$, the computations underpredict the centerline velocity by approximately 5%. For the Reynolds stresses, the biggest discrepancy is on the shear layers at $x/D = 1.0$, for which all three components are higher for the computations.

This discrepancy could be because, initially, the flow emerging from the RANS layer has no resolved scales. Hence, the shear layer is laminar and, perhaps, transitions to turbulence abruptly. Improving the interface between the RANS and NLES regions could help alleviate this problem. For example, a similar method to that of Batten et al. [49] could be used to impose fluctuations in the NLES, based on the RANS layer statistics. This is left as future work.

For the measurements, there is also a spurious overprediction of the normal stress on the centerline at $x/D = 1.0$. Further downstream, the computations show closer agreement with the measurements. For $x/D = 3 \sim 5$, the peak shear-layer stress is within 10% of the measurements.

Figure 9 plots radial profiles of the mean streamwise velocity and the normal stress at axial locations $x/D = 1.0$ to 3.0 for the 6×10^6 and 50×10^6 meshes. Figure 9a shows the time-averaged streamwise velocity, with both meshes giving similar agreement. There is a maximum difference between the two CFD predictions of approximately 5%, in terms of the centerline velocity deficit at $x/D = 2$. However, no measurements are available at this location.

Figure 9b plots radial profiles of the normal stress. The peak values on the jet shear layer are similar for both cases. There is some variation in terms of the spreading rate, particularly at $x/D = 3$. However, generally, both mesh results show similar characteristics. The agreement between the 6×10^6-cell and 50×10^6-cell results suggests that the large scales in the shear layer are dominant for jet flows. This is useful in engineering terms, because it implies that simulations on modest grids can be meaningful.

Figure 10 cross plots the data from Figs. 8 and 9 to show axial profiles from $x/D = 1$ to 5. Figure 10a plots centerline velocity and Fig. 10b plots the normal stress. The top set of curves gives the peak normal stress and the bottom set gives the centerline normal stress. As usual, the lines give the predictions, and the symbols give the measurements. Error bars of $\pm 10\%$ are included on the measurements.

Tables 3 and 4 help to interpret Figs. 8 and 9 quantitatively by listing some errors. Table 3 compares the 12×10^6-cell results to the measurements for different axial locations.

Table 4 includes a summary of the errors at $x/D = 3$ for all simulations (on the different grids) and measurements. Columns headed 6×10^6, 12×10^6, and 50×10^6 show the error of the NLES–RANS simulations when compared with the measurements for the three different meshes. The fifth column (labeled Δ_{max} between CFD) shows the maximum spread for the different NLES–RANS predictions. The final column shows the measurement error. For the mean velocity, this is 5.5% (from the circle-fitting-technique analysis). The normal stress error is larger. This is due to the potential nozzle concentricity issues that, as discussed earlier, tend to influence the Reynolds stresses more than the mean profiles. For the error in the NLES–RANS normal stress, both the average error (discussed in Sec. III) and the error in the peak value on the shear layer are plotted. Errors in the peak values are shown in brackets. The larger average error illustrates that the dominating positional error of the measurements can potentially give misleading values. This is especially true for the Reynolds stresses, for which there are large gradients across a narrow shear layer. Hence, a relatively small positional error (radially) can yield a large average error value. The peak error values

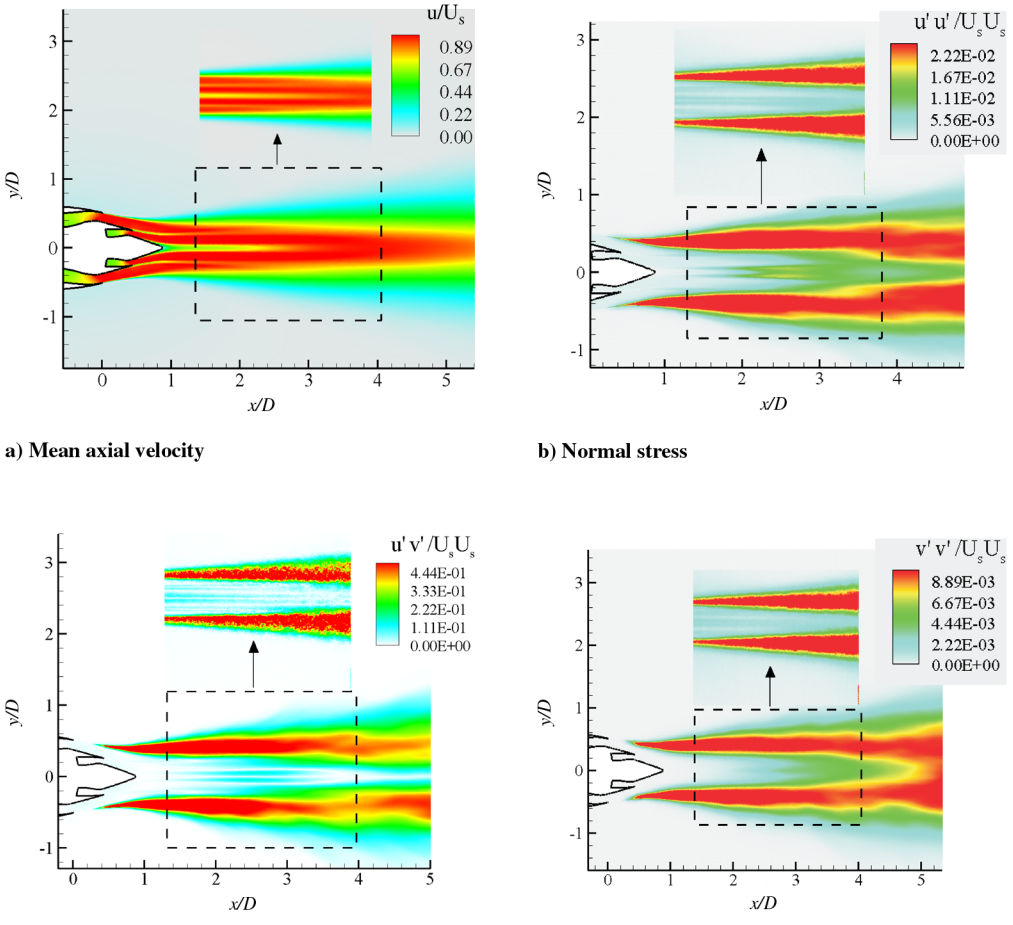

a) Mean axial velocity

b) Normal stress

c) Shear stress

d) Radial stress

Fig. 15 Contours in *x*–*y* plane. Full images show NLES–RANS; insets show PIV.

show that, in terms of the predicted turbulence levels (i.e., ignoring positional errors), the difference between the measurements and the predictions is much lower (around 5%).

Figure 11 plots vorticity contours for all three meshes studied. The top frame shows the 50×10^6-cell case, the middle frame shows the 12×10^6-cell case, and the bottom frame shows the 6×10^6-cell case.

Figure 12 shows the y–z contours of instantaneous streamwise velocity for the three meshes. The top row shows planes at $x/D = 1$, and the bottom row shows planes at $x/D = 2$. From left to right, the frames show the 6×10^6-cell, 12×10^6-cell, and 50×10^6-cell predictions. The figures also show the increased flow physics captured in the 50×10^6-cell case. As with Fig. 11, the largest structures are of similar sizes for all three cases.

Figure 13 plots 12×10^6-cell mesh predictions, both with and without the RANS layer. Because the near-wall mesh is not fine enough in the radial and azimuthal directions for LES, and because the numerical scheme increases smoothing toward the walls, there is no rational basis to expect the NLES alone to be successful. However, it is desirable to observe the effect of the RANS layer. Figure 13a contrasts radial profiles of the mean streamwise velocity at axial locations $x/D = 1.0$, 2.0, and 3.0. Here, solid lines plot the NLES–RANS results, dashed lines plot the NLES results, and symbols plot the measurements. Figure 13a shows that the pure NLES does not predict the velocity deficit on the centerline, which the NLES–RANS and measurements suggest. This indicates that the flow for the NLES is separating toward the rear of the nozzle. This is because the grid is not fine enough for quasi-direct-numerical simulation (the typical near-wall grid requirement needed for LES) and, because there is no RANS layer, the mean flow velocity profile is laminar and, hence, readily separates. This ultimately results in faster radial mixing after the end of the nozzle. This is shown qualitatively in Figs. 13b and 13c, which give density gradient magnitude and instantaneous streamlines. For the simulation with no RANS layer, separation can be seen. Hence, the NLES–RANS method is helpful. It keeps the boundary layer attached, which ultimately gives better agreement with the measurements. Figure 13a shows that at $x/D = 3.0$, the difference between the two computations is decreasing, and by $x/D = 4.0$, both results are similar.

Figure 14 plots the x–y contours of the mean axial velocity for the NLES, NLES–RANS, and PIV measurements. The PIV results show the velocity deficit on the jet centerline for $x/D < 3.0$, indicating that the separation of the flow from the nozzle wall in the NLES simulation is, as expected, nonphysical. Comparison of the contour plots indicates that the PIV has a smaller spreading rate than the NLES–RANS and, hence, so does the LDA. To explore this, Fig. 14c overlays graphs of time-averaged streamwise velocity for the LDA and PIV on the contour plot. Solid lines show the LDA results, and dashed lines show the PIV results. There is a maximum difference in the velocity of approximately $0.05U_{\max}$ at $y/D = 0.5$, and $x/D = 3$.

Figure 15 plots the x–y contours of the mean streamwise velocity and the normal, shear, and radial stresses. The full images show the NLES–RANS results, with the PIV shown in the inset. The images show (as evident in Fig. 13a) that, for the NLES–RANS, the peak Reynolds stresses are overpredicted on the shear layer for $x/D < 2.0$. By $x/D > 3.0$, the shear-layer width and magnitudes for the PIV and computations are similar.

V. Conclusions

A new data set containing LDA and PIV measurements along with large-eddy-resolving computations has been reported for a coflowing short-cowl-nozzle geometry. The Reynolds number is 300,000, and the Mach numbers are representative of realistic engine conditions. The low Reynolds number of the measurements makes the case well suited to the assessment of large-eddy-resolving computational strategies. Also, the nozzle concentricity was successfully controlled to help deal with the emerging metastability issues of jets with coflow. The jet was shown to be axisymmetric in terms of the Reynolds stresses. For computations, the use of a near-wall k–l RANS model for $y^+ < 60$ is found to be helpful in preventing nonphysical separation from the nozzle wall. Blending between the RANS and the large-eddy-resolving regions makes use of the HJ equation. Because the solver being used tends toward being dissipative, the SGS model is abandoned, giving a hybrid NLES–RANS simulation. For the hybrid method, different LES grids were considered, ranging from 6×10^6 to 50×10^6 cells. This gave an approximate doubling of grid nodes in all directions. The results showed encouraging agreement with the measurements, with all meshes showing the same trends. From this, it can be concluded that, for jets, the large scales in the shear layer are dominant; hence, meaningful LES simulations can be gained on relatively modest meshes.

Acknowledgments

Funding from the Engineering and Physical Sciences Research Council (EPSRC) is gratefully acknowledged under grant number GR/T06629/01. P. Tucker gratefully acknowledges his Royal Society Fellowship funding and the support of Rolls–Royce Group, PLC. The authors would like to thank Rolls–Royce Group, PLC for the use of HYDRA. The computations were run on the University of Cambridge supercomputing facility, Darwin, and the U.K. supercomputer, high-end computing terascale resource (HECTOR). The HECTOR computer time was provided through the U.K. Applied Aerodynamics Consortium under EPSRC grant EP/F005954/1 and also through the Cambridge University Gas Turbine Partnership Whole Engine Computational Aeroacoustics Consortium, under grant EP/G027633/1.

References

[1] "European Aeronautics: A Vision for 2020," Advisory Council for Aeronautics Research in Europe, European Commission, Belgium, 2001.

[2] Secundov, A., Birch, S., and Tucker, P., "Propulsive Jets and their Acoustics," *Philosophical Transactions of the Royal Society of London, Series A: Mathematical and Physical Sciences*, Vol. 365, No. 1859, 2007, pp. 2443–2468. doi:10.1098/rsta.2007.2017

[3] Shur, M., Spalart, P., Strelets, M., and Travin, A., "Towards the Prediction of Noise from Jet Engines," *International Journal of Heat and Fluid Flow*, Vol. 24, No. 4, 2003, pp. 551–561. doi:10.1016/S0142-727X(03)00049-3

[4] Shur, M., Spalart, P., and Strelets, M., "Noise Prediction for Increasingly Complex Jets. Part 1: Methods and Tests," *International Journal of Aeroacoustics*, Vol. 4, No. 3, 2005, pp. 213–246. doi:10.1260/1475472054771376

[5] Pope, S., *Turbulent Flows*, Cambridge Univ. Press, New York, 2000.

[6] Suzuki, T., and Colonius, T., "Instability Waves in a Subsonic Round Jet Detected Using a Near-Field Phased Microphone Array," *Journal of Fluid Mechanics*, Vol. 565, Sept. 2006, pp. 1–30. doi:10.1017/S0022112006001613

[7] Andersson, N., Eriksson, L.-E., and Davidson, L., "Effects of Inflow Conditions and Subgrid Model on LES for Turbulent Jets," 11th AIAA Aeroacoustics Conference, AIAA Paper 2005-2925, 2005.

[8] Boersma, B., and Lele, S., "Large Eddy Simulation of a Mach 0.9 Turbulent Jet," 5th AIAA Aeroacoustics Conference, AIAA Paper 1999-1874, May 1999.

[9] Bodony, D., and Lele, S., "Jet Noise Prediction of Cold and Hot Subsonic Jets Using Large Eddy Simulation," 10th AIAA Aeroacoustics Conference, AIAA Paper 2004-3022, May 2004.

[10] Bogey, C., Bailly, C., and Juve, D., "Noise Investigation of a High Subsonic, Moderate Reynolds Number Jet Using a Compressible Large Eddy Simulation," *Theoretical and Computational Fluid Dynamics*, Vol. 16, No. 4, 2003, pp. 273–297. doi:10.1007/s00162-002-0079-4

[11] Eastwood, S. J., Tucker, P. G., Xia, H., and Klostermeier, C., "Developing Large Eddy Simulation for Turbomachinery Applications," *Philosophical Transactions of the Royal Society of London, Series A: Mathematical and Physical Sciences*, Vol. 367, No. 1899, 2009, pp. 2999–3013. doi:10.1098/rsta.2008.0281

[12] Grinstein, F., "Recent Progress on Montone Integrated Large Eddy Simulation of Free Jets," *JSME International Journal*, Vol. 49, No. 4, 2006, pp. 890–898. doi:10.1299/jsmeb.49.890

[13] Tucker, P. G., "Novel MILES Computations for Jet Flows and Noise," *International Journal of Heat and Fluid Flow*, Vol. 25, No. 4, 2004, pp. 625–635. doi:10.1016/j.ijheatfluidflow.2003.11.021

[14] Bodony, D., and Lele, S., "Current Status of Jet Noise Predictions Using Large Eddy Simulation," *AIAA Journal*, Vol. 46, No. 2, 2008, pp. 364–380. doi:10.2514/1.24475

[15] Moinier, P., "Algorithm Developments for an Unstructured Flow Solver," Ph.D. Thesis, Univ. of Oxford, Oxford, 1999.

[16] Kravchenko, A., and Moin, P., "On the Effect of Numerical Errors in Large Eddy Simulation of Turbulent Flows," *Journal of Computational Physics*, Vol. 131, No. 2, 1997, pp. 310–322. doi:10.1006/jcph.1996.5597

[17] Ghosal, S., "An Analysis of Numerical Errors in Large Eddy Simulations of Turbulence," *Journal of Computational Physics*, Vol. 125, No. 1, 1996, pp. 187–206. doi:10.1006/jcph.1996.0088

[18] Grinstein, F., Margolin, L., and Rider, W., *Implicit Large Eddy Simulation*, Cambridge Univ. Press, New York, 2007.

[19] Uzun, A., and Hussaini, Y., "High Frequency Noise Generation in the Near Nozzle Region of a Jet," 12th AIAA Aeroacoustics Conference, AIAA Paper 2006-2499, May 2006.

[20] Bogey, C., Barre, S., and Bailly, C., "Direct Computation of the Noise Generated by Subsonic Jets Originating from a Straight Pipe Nozzle," *International Journal of Aeroacoustics*, Vol. 7, No. 1, 2008, pp. 1–22. doi:10.1260/147547208784079917

[21] Eastwood, S. J., Tucker, P. G., Xia, H., Carpenter, P., and Dunkley, P., "Comparison of LES to LDA and PIV Measurements of a Small Scale High Speed Coflowing Jet," 14th AIAA/CEAS Aeroacoustics Conference, AIAA Paper 2008-2981, May 2008.

[22] Andersson, N., Eriksson, L.-E., and Davidson, L., "LES Prediction of Flow and Acoustic Field of a Coaxial Jet," 11th AIAA Aeroacoustics Conference, AIAA Paper 2005-2884, May 2005.

[23] Bogey, C., Barre, S., and Bailly, C., "Direct Computation of the Noise Generated by a Hot Coaxial Jet," 13th AIAA Aeroacoustics Conference, AIAA Paper 2007-3587, May 2007.

[24] Mihaescu, M., Szasz, R., and Fuchs, L., "Numerical Investigation of the Acoustics of a Coaxial Nozzle," 43rd AIAA Aerospace Sciences Meeting and Exhibit, AIAA Paper 2005-420, Jan. 2005.

[25] Shur, M., Spalart, P., Strelets, M., and Garbaruk, A., "Further Steps in LES Based Noise Prediction for Complex Jets," 44th AIAA Aerospace Sciences and Meeting Exhibit, AIAA Paper 2006-485, Jan. 2006.

[26] Vuillot, F., Lupoglazoff, N., and Rahier, G., "Double Stream Nozzle Flows and Noise Computations and Comparisons to Experiments," 46th AIAA Aerospace Sciences Meeting and Exhibit, AIAA Paper 2008-9, Jan. 2008.

[27] Yan, J., Tawackolian, K., Michel, U., and Thiele, F., "Computation of Jet Noise using a Hybrid Approach," 13th AIAA Aeroacoustics Conference, AIAA Paper 2007-3621, May 2007.

[28] Viswanathan, K., Shur, M., Spalart, P., and Strelets, M., "Flow and Noise Predictions for Single and Dual Stream Beveled Nozzles," *AIAA Journal*, Vol. 46, No. 3, 2008, pp. 601–626. doi:10.2514/1.27299

[29] Paliath, U., and Morris, P., "Prediction of Noise from Circular Beveled Nozzles," 11th AIAA Aeroacoustics Conference, AIAA Paper 2005-3096, May 2005.

[30] Uzun, A., and Hussaini, Y., "Noise Generation in the Near Nozzle Region of a Chevron Nozzle Jet Flow," 13th AIAA Aeroacoustics Conference, AIAA Paper 2007-3596, May 2007.

[31] Xia, H., Tucker, P. G., and Eastwood, S. J., "Towards Jet Flow LES of Conceptual Nozzles for Acoustic Predictions," 46th AIAA Aerospace Sciences Meeting and Exhibit, AIAA Paper 2008-, Jan. 2008.

[32] Spalart, P., "Strategies for Turbulence modeling and Simulations," *International Journal of Heat and Fluid Flow*, Vol. 21, No. 3, 2000, pp. 252–263. doi:10.1016/S0142-727X(00)00007-2

[33] Wolfshtein, M., "The Velocity and Temperature Distribution on One Dimensional Flow with Turbulence Augmentation and Pressure Gradient," *International Journal of Heat and Mass Transfer*, Vol. 12, No. 3, 1969, pp. 301–318. doi:10.1016/0017-9310(69)90012-X

[34] Xia, H., Tucker, P. G., and Eastwood, S. J., "Large Eddy Simulations of Chevron Jet Flows with Noise Predictions," *International Journal of Heat and Fluid Flow*, Vol. 30, No. 6, 2009, pp. 1067–1079. doi:10.1016/j.ijheatfluidflow.2009.05.002

[35] Birch, S., Khritov, K., Maslov, V. A., Mironov, A., and Secundov, A., "An Experimental Study of Flow Asymmetry in Co-Axial Jets," 11th AIAA Aeroacoustics Conference, AIAA Paper 2005-2845, May 2005.

[36] Dawes, W., "Turbomachinery Computational Fluid Dynamics. Asymptotes and Paradigm Shifts," *Philosophical Transactions of the Royal Society of London, Series A: Mathematical and Physical Sciences*, Vol. 365, No. 1859, 2007, pp. 2553–2585. doi:10.1098/rsta.2007.2021

[37] Spalart, P., and Bogue, D., "The Role of CFD in Aerodynamics, Off-Design," *The Aeronautical Journal*, Vol. 107, No. 1072, 2003, pp. 323–329.

[38] Tucker, P. G., "Turbulence modeling of Problem Aerospace Flows," *International Journal for Numerical Methods in Fluids*, Vol. 51, No. 3, 2006, pp. 261–283. doi:10.1002/fld.1120

[39] Bridges, J., and Wernet, M., "Effect of Temperature on Jet Velocity Spectra," 13th AIAA Aeroacoustics Conference, AIAA Paper 2007-3628, 2007.

[40] Bridges, J., and Wernet, M., "Turbulence Asociated with Boradband Shock Noise in Hot Jets," 14th AIAA/CEAS Aeroacoustics Conference, AIAA Paper 2008-2834, May 2008.

[41] Yang, K., and Ferziger, J., "Large Eddy Simulation of Turbulent Obstacle Flow Using a Dynamics Subgrid Scale Model," *AIAA Journal*, Vol. 31, No. 8, 1993, pp. 1406–1413. doi:10.2514/3.49081

[42] Tucker, P. G., and Davidson, L., "Zonal k–l Based Large Eddy Simulations," *Computers and Fluids*, Vol. 33, No. 2, 2004, pp. 267–287. doi:10.1016/S0045-7930(03)00039-2

[43] Zhong, B., and Tucker, P., "k–l Based Hybrid LES/RANS Approach and its Application to Heat Transfer Simulation," *International Journal for Numerical Methods in Fluids*, Vol. 46, No. 10, 2004, pp. 983–1005. doi:10.1002/fld.782

[44] Roe, P., "Approximate Riemann Solvers, Parameter Vectors, and Difference Solvers," *Journal of Computational Physics*, Vol. 135, No. 2, 1997, pp. 250–258. doi:10.1006/jcph.1997.5705

[45] Morgan, K., Peraire, J., and Hassan, O., "The Computation of Three Dimensional Flows Using Unstructured Grids," *Computer Methods in Applied Mechanics and Engineering*, Vol. 87, No. 2–3, 1991, pp. 335–352. doi:10.1016/0045-7825(91)90012-U

[46] Ciardi, M., Klein, M. P. S., and Dawes, W., "A Dynamic Finite Volume Scheme for Large Eddy Simulation on Unstructured Grids," *Journal of Computational Physics*, Vol. 210, No. 2, 2005, pp. 632–655. doi:10.1016/j.jcp.2005.04.025

[47] Tucker, P. G., Coupland, J., Eastwood, S. J., Xia, H., Liu, Y., Jefferson-Loveday, R., and Hassan, O., "Contrasting Code Performances for Computational Aeroacoustics of Jets," 12th AIAA/CEAS Aeroacoustics Conference, AIAA Paper 2006-2672, May 2006.

[48] Moulinec, C., Benhamadouche, S., Laurence, D., and Peric, M., "LES in a U-Bend Pipe Meshed by Polyhedral Cells," *Engineering Turbulence Modelling and Experiments*, Vol. 6, Elsevier, Amsterdam, 2005, pp. 237–246.

[49] Batten, P., Goldberg, U., and Chakravarthy, S., "Interfacing Statistical Turbulence Closures with Large Eddy Simulation," *AIAA Journal*, Vol. 42, No. 3, 2004, pp. 485–492. doi:10.2514/1.3496

T. Lyrintzis
Associate Editor